Side-Wall Effects on the Global Stability of Swept and Unswept Supercritical Wings at Buffet Conditions

Andrea SANSICA [(1)], HASHIMOTO Atsushi [(1)], KOIKE Shunsuke[(1)] and KOUCHI Toshinori[(2)]
[(1)]*Japan Aerospace Exploration Agency, 7-44-1 Jindaiji Higashi-machi, Chofu-shi, Tokyo 182-8522, Japan*
[(2)]*Dept. of Mech. and Systems Engineering, Faculty of Engineering, Okayama University, Okayama, 700-8530 Japan*

ABSTRACT

A fully three-dimensional (3D) RANS-based global stability analysis is performed on wings in the presence of side-walls to study the complex interaction between buffet shock-oscillations, buffet cells and corner separations. A validation of both the nonlinear and linear stability analysis solvers is given for a two-dimensional (2D) incompressible laminar cylinder and for turbulent transonic buffet on a 2D OAT15A airfoil. The numerical setup is based on the experiments conducted at JAXA 0.8 m $\times$ 0.45 m high Reynolds number transonic wind tunnel on a 2D Common Research Model (CRM) profile. The CRM profile is extruded in the spanwise direction and flash mounted on lateral walls at its extremities. An unswept and a swept configuration at sweep angle of 10° are considered. The effect of the angle of attack (AoA) is studied for both configurations by selecting AoA = 4 and 7°. The RANS solutions are compared against the experimental oil-flow visualizations. Despite some differences in terms of size of the corner separation and shock locations, the main flow features are captured. For the unswept case, the results show that the separation in the middle wing section and corners increases with the AoA. Since the flow slows down near the side-walls, the shock is weakened and moves upstream towards the leading edge. When a sweep angle is applied, the flow is distorted by a crossflow velocity component that causes the corner separations to increase or decrease depending on the boundary-layer thickness of the secondary flow created in the wing spanwise direction. Linear global stability calculations carried out on the unswept wing at the lowest AoA show the presence of a 2D oscillatory mode at $St \approx 0.06$ that is spatially localized on the shock. Another unstable mode at higher frequencies ($St \approx 0.1$) is located near the corner separations and perturbation packets travel downstream along the shear-layer. For the highest AoA, the 2D mode no longer exists and two 3D modes at higher frequencies appear ($St \approx 0.07$ and $St \approx 0.2$). These modes are organized in spanwise perturbation wavepackets generated from the corner separation and convected downstream towards the wing middle section. In the separated region in the wing mid-section, the perturbations travel upstream from the trailing-edge towards the shock. Future investigations will focus on the effect of the sweep angle and detection of buffet cells.

1. Introduction

In high speed flight, shock-wave/boundary-layer interaction (SWBLI) may have dramatic consequences on the aero-thermodynamic loads and airplane performance. Near the interaction region, flow separation, transition to turbulence, unsteadiness and three-dimensional (3D) effects can simultaneously occur, actively changing the pressure and skin friction distributions of the flow field. For these reasons, SWBLI has been one of the most important topics within the aeronautical scientific community in the past 70 years [12]. For transonic airfoils an additional complication is represented by the self-sustained shock-wave oscillations of the so-called buffet phenomenon. This instability is characterized by low-frequency oscillations of the same order as the modal structural ones, resulting in the limitation of the flight envelope as well as representing a cause for potential failure to fatigue. The extensive reviews on transonic buffet [24, 14], that discuss the progress made since its first experimental evidence in 1947 [19], reveal that two widely accepted but conflicting interpretations of the governing mechanisms exist. The first theory explains the periodic shock oscillations as the consequence of a feedback mechanism involving downstream traveling pressure waves emanated from the shock foot and upstream traveling pressure waves generated at the trailing edge, that provide energy to the shock and close the feedback loop [23]. The second theory shows instead that a global instability produces pressure perturbations in the direction normal to the profile and directly transfer energy along the shock [7]. Despite the growing body of literature on the subject, a precise understanding of the complex underlying physical mechanisms is therefore still lacking. Another relevant and not fully understood aspect of the buffet phenomenon concerns its intrinsic 3D character. Experimental investigations have clearly shown the existence of a spanwise outboard propagation of the so-called “buffet cells” [10, 22, 38] and although their main features have been documented, many aspects are still un-

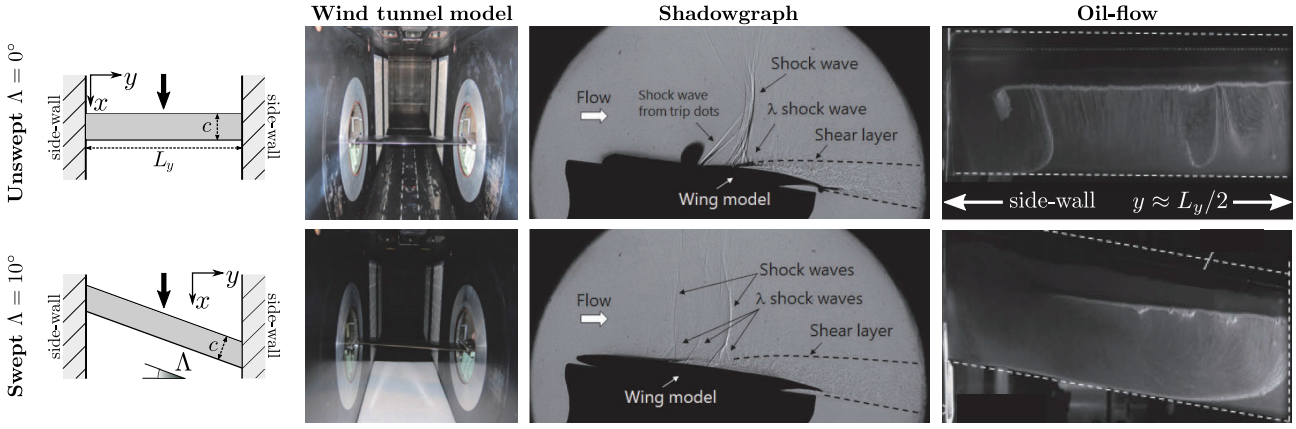

Figure 1: Schematic top view (first column, the thick arrows indicate the flow direction), wind tunnel models (second column, flow direction in the outward normal-to-the-paper direction), shadowgraph images (third column, flow direction from left to right) and oil-flow visualization (fourth column, flow direction from top to bottom) at M=0.72 and AoA = 7° for the unswept (first row) and Λ=10° swept (second row) models. Adapted from [21].

clear. The numerical work has been extensively focusing on two-dimensional (2D) configurations but recent 3D calculations have been carried out on both full-aircraft or extruded in the spanwise direction [11, 16, 34, 20, 27] configurations and have verified the appearance of buffet cells at different levels of simulation fidelity. Global stability analysis has also been employed to better understand the mechanisms governing the origin of buffet cells [8, 30, 40] on swept wings but many aspects of the intrinsic three-dimensionality still need to be investigated.

The present work aims at performing a fully-3D global stability analysis study on unswept and swept wings in the presence of side-walls. The paper is presented as follows: a brief description of the experimental setup and results is given in Sec. 2; the governing equations and the stability problem are formulated in Sec. 3; the numerical method is presented in Sec. 4; nonlinear Reynolds-Averaged-Navier-Stokes (RANS) calculation and global stability results are described in Sec. 5; the conclusions and perspectives for future work are summarized in Sec. 6. A 2D validation for both nonlinear and linear stability analysis in given in the Appendix A.

2. Experimental Investigations

The effects of side-walls on a 2D extruded wing were experimentally investigated at JAXA 0.8 m × 0.45 m high Reynolds number transonic wind tunnel (JTWT2). A brief summary of the experimental setup and results is here described. The wing cross-section is a NASA Common Research Model (CRM) blunt trailing-edge profile [1] with chord $c = 0.10\,m$ and span width $L_z = 0.45\,m$. Two separately manufactured models were considered for unswept and swept configurations. The sweep angle (Λ) for the swept model was $\Lambda = 10^\circ$. A schematic representation of the unswept and swept configurations is represented in figure 1 (first column). Both models were flash-mounted to the wind tunnel side-walls on both wing extremities (see second column of figure 1). The effect of different Mach numbers (M) and angles of attack (AoA) on turbulent shock-induced separation and shock-wave oscillations was studied via high-speed camera shadowgraph, oil flow visualizations and pressure measurements at the mid-span wing section. Different types of shock-wave oscillations were classified depending on the interaction with shock-induced and corner separations. For the $M = 0.72$ and AoA$= 7^\circ$ case, the shadowgraph images (third column of figure 1) and oil-flow visualization (fourth column of figure 1) are reported. At this condition, the frequency of the shock oscillations is $f = 170\,Hz$ and $f = 244\,Hz$ for the unswept and swept wings, respectively. Further information about the experimental setup and results can be found in [21].

3. Problem Formulation

The compressible 3D RANS equations for a perfect gas can be written using Boussinesq hypothesis in the non-dimensional form as:

$$\frac{\partial \mathbf{q}}{\partial t} = \mathscr{N}(\mathbf{q}), \tag{1}$$

where $\mathbf{q} = [\rho, \rho\mathbf{u}, \rho E, \rho\nu_t]^T$ is the state vector in the conservative form (with ρ, $\mathbf{u}$, E and ν_t being fluid density, velocity vector, total energy, and kinematic turbulent viscosity, respectively) and t is the time. The differential nonlinear RANS operator $\mathscr{N}$ can be explicitly expanded as

$$\mathscr{N}(\mathbf{q}) = -\boldsymbol{\nabla}\begin{pmatrix} \rho\mathbf{u} \\ \rho\mathbf{u}\otimes\mathbf{u} + p\mathbf{I} - \boldsymbol{\tau} - \boldsymbol{\tau}_R \\ \rho E\mathbf{u} + p\mathbf{u} - \boldsymbol{\tau}\mathbf{u} - \boldsymbol{\tau}_R\mathbf{u} + \mathbf{q} + \mathbf{q}_R \\ \rho\nu_t\mathbf{u} - \frac{\mu+\rho\nu_t}{\sigma_M}\boldsymbol{\nabla}\nu_t + \mathscr{S}_M \end{pmatrix} \tag{2}$$

with

$$\begin{aligned} p &= (\gamma-1)\rho E - \tfrac{1}{2}\mathbf{u}\cdot\mathbf{u} \\ \boldsymbol{\tau} &= \mu\left[(\boldsymbol{\nabla}\otimes\mathbf{u}+\boldsymbol{\nabla}\otimes\mathbf{u}^T)-\tfrac{2}{3}(\boldsymbol{\nabla}\cdot\mathbf{u})\mathbf{I}\right] \\ \boldsymbol{\tau}_R &= \mu_t\left[(\boldsymbol{\nabla}\otimes\mathbf{u}+\boldsymbol{\nabla}\otimes\mathbf{u}^T)-\tfrac{2}{3}(\boldsymbol{\nabla}\cdot\mathbf{u})\mathbf{I}\right] \\ \mathbf{q} &= -\tfrac{\mu C_p}{Pr}\boldsymbol{\nabla}T \\ \mathbf{q}_R &= -\tfrac{\mu_t C_p}{Pr_t}\boldsymbol{\nabla}T \end{aligned} \tag{3}$$

being p the pressure, $\boldsymbol{\tau}$ the stress tensor, $\boldsymbol{\tau}_R$ the Reynolds stress tensor, C_p the heat capacity at constant pressure, μ the dynamic viscosity, μ_t the eddy viscosity, Pr and Pr_t the classical and turbulent Prantdl numbers, T the temperature, $\mathbf{q}$ the heat flux and $\mathbf{q}_R$ the flux of diffusion of turbulent enthaply. The Prandtl numbers are considered constant and equal to $Pr = 0.72$ and $Pr_t = 0.90$. The dynamic viscosity is assumed to follow Sutherland's law as

$$\mu = T^{3/2}\frac{1+T_s}{T+T_s} \tag{4}$$

where $T_s = 110.4K/T^*_{i,\infty}$, with $T^*_{i,\infty}$ the dimensional free-stream stagnation temperature (the superscript * indicates dimensional quantities). The array of the streamwise, vertical and transverse directions is indicated by $\mathbf{x} = [x,y,z]^T$. Note that all variables are Reynolds averaged, except for $\mathbf{u}$ and E that are Favre (density-weighted) averaged. The formulations of the coefficient σ_M and the turbulent source terms $\mathscr{S}_M$ depend on the turbulence model.

3.1. Stability Problem

The stability problem is based upon the use of the linearized RANS equations. The first step to obtain this linearized set of equations is to assume that the nonlinear system in Eq. (1) admits an equilibrium solution, $\mathbf{q}_b$, defined by $\mathscr{N}(\mathbf{q}_b) = 0$ and referred to as fixed point or base flow. In this case, the steady RANS solution corresponds to the base flow. The standard small perturbation technique is used to decompose the instantaneous flow into base flow and small disturbances $\mathbf{q}(\mathbf{x},t) = \mathbf{q}_b(\mathbf{x}) + \varepsilon\mathbf{q}'(\mathbf{x},t)$, with $\varepsilon \ll 1$. By assuming that the perturbations are infinitesimal, all nonlinear fluctuating terms are ignored and the linearized RANS equations can be written as

$$\frac{\partial \mathbf{q}'}{\partial t} = \mathscr{L}\mathbf{q}', \tag{5}$$

where $\mathbf{q}' = \left[\rho', \rho'\mathbf{u}_b + \rho_b\mathbf{u}', \rho' E_b + \rho_b E', \rho'\nu_{t,b} + \rho_b\nu_t'\right]^T$ is the state vector of conservative perturbation variables and $\mathscr{L} = \partial\mathscr{N}/\partial\mathbf{q}\,|_{\mathbf{q}_b}$ is the Jacobian operator obtained by linearizing the RANS operator $\mathscr{N}$ around the base flow $\mathbf{q}_b$. By choosing the normal mode or wave solution $\mathbf{q}'(\mathbf{x},t) = \widehat{\mathbf{q}}(\mathbf{x})\exp(\lambda t) + c.c.$, the eigenproblem $\mathscr{L}\widehat{\mathbf{q}} = \lambda\widehat{\mathbf{q}}$ is obtained. The complex eigenvalue can be split in its real and imaginary parts $\lambda = \sigma + i\omega$, where σ is the temporal growth rate and ω the pulsation. While the pulsation characterizes the oscillatory behavior, the temporal growth rate indicates whether the equilibrium state bifurcates to another solution. This bifurcation is expressed in a linear framework by the existence of eigenmodes with a corresponding positive growth rate.

4. Numerical Method

While the calculation of the base flow solutions is carried out by using a classical RANS (nonlinear) solver, the global stability analysis requires of a RANS linearized solver. The characteristics and numerical strategies used for both solvers are described below.

4.1. Nonlinear Solver

As RANS nonlinear solver, JAXA's unstructured-grid flow solver FaSTAR [18, 20] is used. The governing equations are the compressible Navier-Stokes equations. The cell-center finite volume method is used for the discretization. The numerical flux is computed by the HLLEW scheme [29]. The WGG is used for the gradient computation. The dual-time stepping [41] method is used to perform an accurate time calculation with an implicit time integration scheme. The LU-SGS [35] scheme is used for the pseudo time sub-iteration and the physical time derivative is approximated by the three-point backward difference. The Spalart-Allmaras turbulence model [37] with rotation correction (SA-R) [9] and quadratic constitutive relation 2000 version [36] is used to close the averaged Reynolds stresses. The trip term ft_2 is also ignored (SA-R-noft2). The boundary conditions used are: no-slip velocity and adiabatic temperature on the profile and side-walls; far-field boundary conditions are employed at the lateral boundaries and the AoA is applied at the inflow of the numerical domain. All steady solutions are computed by using a large Courant-Friedrichs-Lewy (CFL) number equal to 10. The selective frequency damping (SFD) method [31, 2] is used to further converge the steady fixed point solution and filter any possible unsteadiness.

4.2. Linearized Solver

The expression of $\mathscr{L}\mathbf{q}'$ is extremely complicated and would mean a lengthy implementation / modification of the existing nonlinear version of FaSTAR. To avoid this, a strategy based on a finite difference method consists of using the nonlinear solver in a black box manner and approximate $\mathscr{L}\mathbf{q}'$ via repeated evaluation of the residual function $\mathscr{N}(\mathbf{q})$. A Taylor series expansion with a first order approximation allows then

$$\mathscr{L}\mathbf{q}' = \frac{1}{\varepsilon}[\mathscr{N}(\mathbf{q}_b + \varepsilon\mathbf{q}') - \mathscr{N}(\mathbf{q}_b)], \tag{6}$$

with ε being a small constant. This method and selection of the ε constant are further discussed in [39, 28]. A matrix-free method [13, 4] is used to solve the eigenproblem $\mathscr{L}\widehat{\mathbf{q}} = \lambda\widehat{\mathbf{q}}$. Being $\mathbf{L}$ the discrete form of $\mathscr{L}$, it

is possible to introduce the exponential propagator $\mathbf{M} = \exp(\mathbf{L}\Delta T)$ that linearly advances the perturbation solution in time as $\mathbf{q}'(t^{n+1}) = \mathbf{M}\mathbf{q}'(t^n)$, with $t^{n+1} = t^n + \Delta T$. An Arnoldi algorithm [3, 25, 5] is coupled to the linearized solver [26, 17, 32] to extract the leading eigenmodes of $\mathbf{M}$. All conservative perturbation quantities are let evolving in time, including the perturbation eddy viscosity in a "non-frozen turbulence" fashion.

A validation of the linearized solver is given in the Appendix A for a 2D laminar incompressible cylinder and a 2D turbulent transonic buffet case.

5. Side-Wall Effects on the Global Stability of Transonic Buffet

The geometry in exam consists of a 2D CRM profile extruded in the spanwise direction with both ends flash mounted on vertical side-walls. Two wing configurations are studied: an unswept wing, that is simply extruded in the side-wall normal direction, and a swept one, for which the extrusion is done by applying a sweep angle of $\Lambda = 10^\circ$. For each configuration, two angles of attack were considered as AoA $= 4$ and 7°. An O-grid of about 10 millions cells was similarly generated for both unswept and swept configurations. The domain inflow is set to be $3\,m$ upstream of the profile in order to obtain a boundary-layer 99% thickness of $34\,mm$ at $150\,mm$ upstream of the profile leading edge, based on some previous experimental measurements. It should be noted that the actual experiments carried out for this study did not report any measurement of the boundary-layer thickness on the side-walls. The cells in the extruded direction are symmetrically distributed with respect to the center plane in the spanwise direction and clustered near the side-walls. Due to the symmetry of the solution for the unswept configuration, only half of the domain was considered and symmetric boundary conditions applied. The results are presented in two separated sections: the first one reporting the base flow solutions obtained with FaSTAR nonlinear solver, and the second one where the global stability analysis carried out with FaSTAR linearized solver is shown.

5.1. Base Flow Solutions

The 3D steady solutions are discussed for the unswept and swept configurations separately. It is important to notice that the solutions for the unswept configurations were calculated on half of the domain and symmetry was applied. The visualization are reported on the full wing by simply mirroring the solution.

- *Unswept Wing:* $\Lambda = 0^\circ$

Fig. 2 shows the 3D visualization for the AoA $= 4$ and 7° cases (top-row and bottom-row, respectively). While the middle plots show the entire wing, the lateral plots zoom on the wing extremities, providing a view of the flow characteristics on the lateral walls. On both wing and lateral walls, the streamlines (thin black solid lines) are over-imposed to the pressure contours. Iso-surfaces of zero-streamwise velocity (in gray) are added to identify the recirculation regions. Sonic Mach iso-lines (thick white solid lines) are also shown to indicate the shock. For both AoA, large corner separations appear and the flow slowly recirculates on both wing and side-walls. The flow gradually slows down towards the walls, the shock-wave weakens and moves upstream. The corner separations increases in size for increasing AoA, but a similar structure is preserved. In the middle section, for the lowest AoA the flow is only separated in a small region downstream of the shock-wave and on the trailing-edge. For the highest AoA, the flow in the wing center is instead fully separated from shock front to trailing edge.

- *Swept Wing:* $\Lambda = 10^\circ$

Similarly to the unswept wing, the flow for the swept configuration at $\Lambda = 10^\circ$ is visualized in Fig. 3. When a sweep angle is applied, a crossflow velocity component is introduced. This secondary flow in the wing spanwise direction is formed and the thinner (thicker) boundary-layer on the inboard (outboard) side-wall is less (more) prone to separate. For this reason, smaller (larger) corner separation exists on the inboard (outboard) side-wall. Similarly to the unswept wing, the corner separations increase for increasing AoA and the flow is fully-separated only for the highest AoA.

- *Experimental Comparisons*

The RANS solutions are compared against the experimental oil-flow visualizations in Fig. 4. Although the main features are reproduced in the numerical results, it is important to notice that the corner separations are over-estimated in the RANS solutions. This could be due to the fact that the boundary-layer thickness set in the RANS calculations may be different from the experimental one. Also, suction was applied on the side-walls during the experiments. Some turbulence sensitivity tests (not shown here) show that the corner separations are reduced and more similar to the experimental ones when EARSM or SST models are used. Future investigations on the side-wall effects need to be addressed. By comparing the shock locations obtained on different sections of the wings for both unswept and swept configurations (Fig. 5), it is possible to see that the shock location also present several differences. The current configurations is very challenging to be accurately reproduced by the numerical simulations. The co-existence of large separations, shocks and turbulent boundary-layers make the comparisons very complex. However, the main flow features seem to be reproduced and these base flows are used to carry out the global stability analyses.

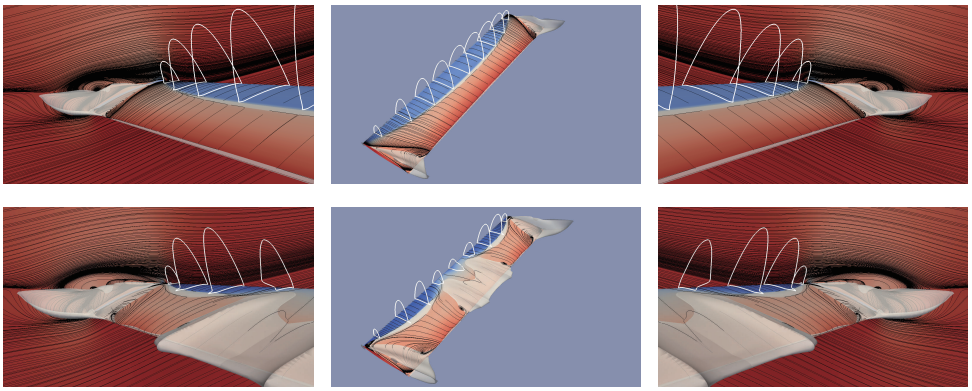

Figure 2: RANS solutions for the unswept ($\Lambda = 0°$) wing configuration at AoA $= 4$ (top plots) and $7°$ (bottom plots).

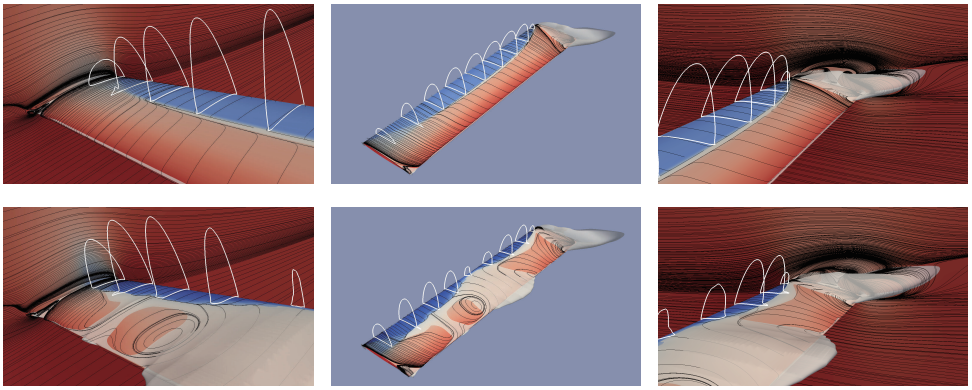

Figure 3: RANS solutions for the swept ($\Lambda = 10°$) wing configuration at AoA $= 4$ (top plots) and $7°$ (bottom plots).

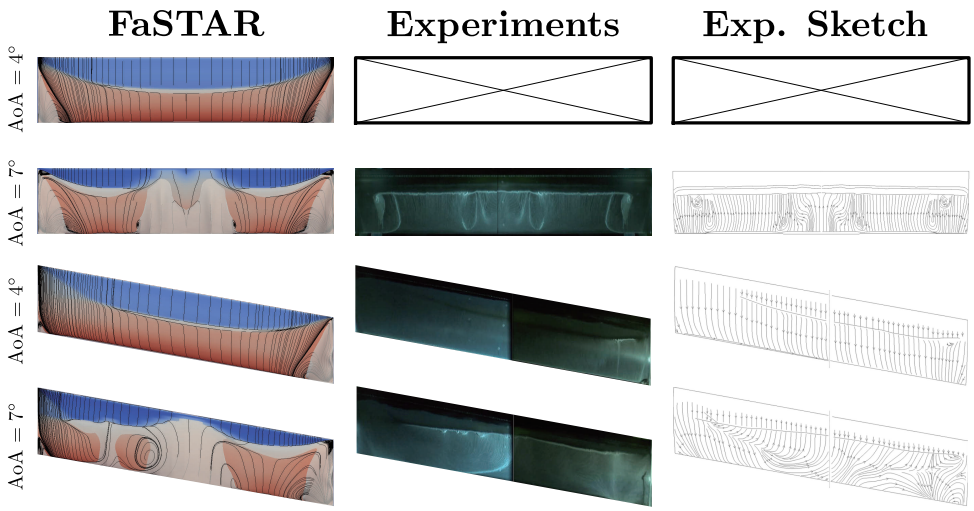

Figure 4: Comparison between RANS solutions and experimental oil-flow visualizations. A sketch of the oil flow visualizations reporting the experimental streamlines is also added. Unswept wing at AoA $= 4°$ was not investigated experimentally. Experimental results from [21].

5.2. Global Stability Analysis

The global stability analysis was carried out only for the unswept wing configuration and the swept wing remains to be studied.

The eigen-spectrum obtained for the AoA $= 4$ and $7°$ cases (blue and red circles, respectively) are reported in Fig. 6. Due to not sufficiently well converged base flow

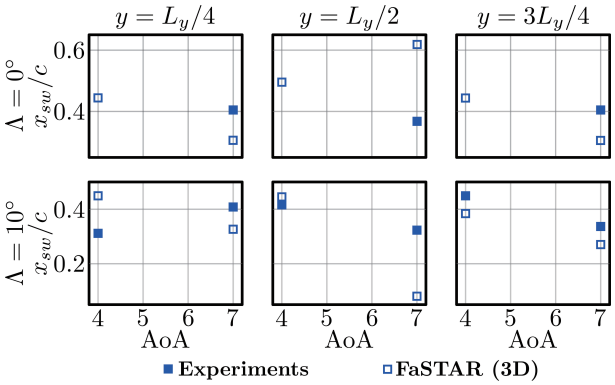

Figure 5: Comparison between RANS and experimental shock locations. Experimental results from [21].

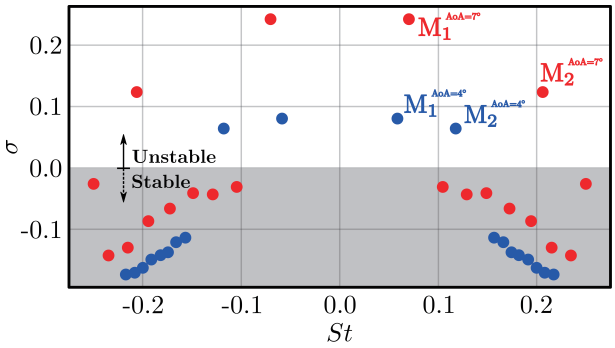

Figure 6: Unswept wing configuration. Global stability analysis eigen-spectra for AoA = 4 and 7° cases (blue and red circles, respectively).

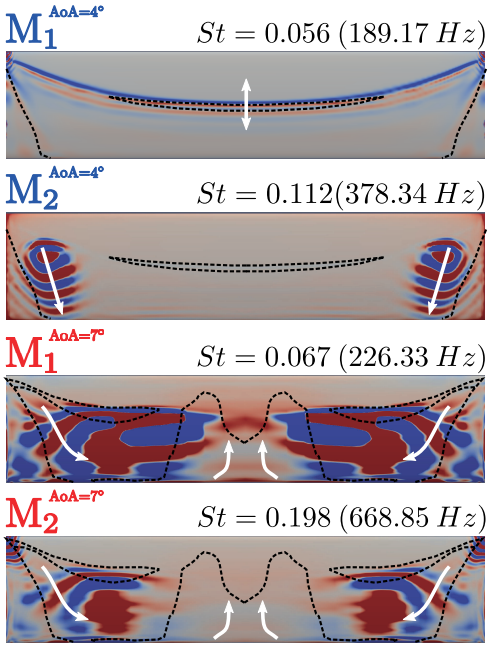

Figure 7: Unswept wing configuration. Global stability eigenmodes for AoA = 4 and 7° cases (top two plots and bottom two plots, respectively).

solutions, some spurious modes appeared but were ignored and not reported in the figure. Future work includes a better convergence of the base flows to remove these spurious modes from the stability calculations.

For the lowest AoA, two unstable modes were found at $St = 0.056$, or dimensional frequency of $f \approx 190\,Hz$ (indicated as $M_1^{AoA=4°}$ in the figure), and $St = 0.112$, or dimensional frequency of $f \approx 380\,Hz$ (indicated as $M_2^{AoA=4°}$ in the figure). The corresponding eigenmodes are reported in the first two top-plots of Fig. 7, where white arrows are added to show the propagation directions and black dashed lines indicate the zero-streamwise velocity iso-lines from the base flow solution. The low-frequency $M_1^{AoA=4°}$ mode is essentially 2D and localized on the shock foot. This mode corresponds to the shock-oscillations buffet mode. The higher-frequency $M_2^{AoA=4°}$ mode presents instead an instability coming from the corner separation and moves downstream along the shear-layer.

For the highest AoA, two high-frequency modes at $St = 0.067$ and $St = 0.198$ are found to be unstable. The corresponding eigenmodes in the last two bottom-plots of Fig. 7 show that the 2D mode no longer exists. Both modes are 3D and organized in perturbation structures that move from the corner separation towards the wing center. At lower amplitudes, the perturbations travel upstream from the trailing edge towards the shock in the wing mid-section, where full separation exists.

Although 3D structures appear and the corresponding non-dimensional frequencies match those of buffet cells shown in the literature, it is difficult to conclude that they are indeed buffet cells. The buffet cells wavelengths have normally been reported to be around one profile chord, but the presence of side-walls and corner separations may affect this. Future investigations on swept configurations might elucidate this point.

6. Conclusions and Future Work

The interaction between transonic buffet shock oscillations, corner separation and spanwise buffet cells is studied for an extruded 2D Common Research Model (CRM) profile and flash mounted on lateral walls at its extremities. Both unswept and swept configurations at different angles of attack are considered. The numerical setup is based on the experiments carried out at JAXA 0.8 m × 0.45 m high Reynolds number transonic wind tunnel. Although some differences exist with the experimental results, the RANS solutions capture the main flow features. Corner separations appear on the side-walls and for high angles of attack the flow in the wing mid-section fully

separates from the shock-front to the trailing edge. Due to the flow slowing down near the side-walls, the shock is weaker in those regions and moves upstream towards the leading edge. When a sweep angle is applied, the cross-flow velocity component introduced in the swept configurations induces a secondary flow in the direction of sweep and large separation due to a thick boundary-layer appears on the outboard corner. A linearized version of FaSTAR has been developed and validated. The previously described RANS solutions are used as base flows to perform global stability analysis. The linear global stability calculations on the unswept wing show the existence of a 2D oscillatory mode at $St \approx 0.06$ that is spatially localized on the shock and corresponds to 2D buffet shock oscillations. A second unstable mode at $St \approx 0.1$ is located near the corner separations and consists of downstream traveling perturbation packets that move along the shear layer. When the angle of attack is increased, two 3D unstable modes appear and both are related to downstream traveling perturbations that move away from the wall towards the wing center and upstream traveling perturbations that move from the trailing edge towards the shock in the fully separated middle section. Although convection features and non-dimensional frequencies are close to those reported in the literature, it is difficult to conclude that these structures correspond to buffet cells. Fig. 8 shows a schematic representation of unswept and swept wings in the presence of side-walls. It is well known that a cross-flow velocity component is needed to generate convected buffet cells. This cross-flow component is naturally added in the presence of swept wing configurations. However, in the case of an extruded wing flash mounted on both extremities on side-walls, the existence of corner separations produces cross flow velocity components near the side-walls. This seems to cause the convection of structures moving away from the side-walls when the corner separation is sufficiently large even for unswept wings. The interaction/competition of these corner separation cross flow components and the main cross flow in swept wings is part of future investigations. As well as assessing grid and turbulence model sensitivity, further work also includes a better convergence of the RANS base flow solutions, addressing the side-wall treatment issue and study the effect of numerically reproducing the whole test section (top and bottom walls included).

Acknowledgments

The experimental work was supported by JSPS KAKENHI Grant Number JP18H03814. The experimental results of this study are based on the JAXA wind tunnel test TWT2-18-07. We would like to express our gratitude to those involved in the JAXA Aerodynamic Research Unit who supported us during the experiments.

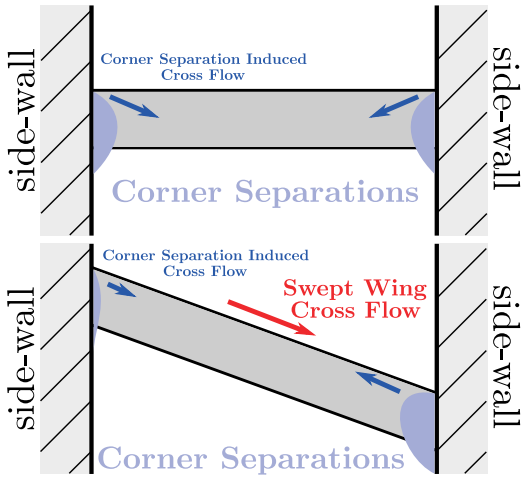

Figure 8: Schematics of corner separation induced cross flow and swept wing cross flow for unswept and swept configurations.

Appendix A: Linearized Solver Validation

In order to provide a validation for both nonlinear and linearized solvers, two validation test cases are selected. The results obtained with FaSTAR are compared against those of Giannetti & Luchini [15] for a 2D laminar incompressible cylinder and against those of Sartor *et al.* [33] for a 2D turbulent transonic buffet case.

- 2D Laminar Incompressible Cylinder

The laminar incompressible flow past a 2D cylinder remains stable and symmetric up to the critical Reynolds number of $Re \approx 47$ (based on free-stream velocity and cylinder diameter). If the Reynolds number is further increased, the flow undergoes a Hopf supercritical bifurcation, the cylinder wake becomes unsteady and a periodic self-sustained von Kármán vortex street is shed behind the body. To approximate incompressible conditions, the Mach number was set to $M = 0.1$ in FaSTAR. The numerical fluxes are calculated with the Roe scheme. The GLSQ is used for the gradient computation. The dual-time stepping method is used to perform an accurate time calculation with an implicit time integration scheme. The LU-SGS scheme is used for the pseudo time sub-iteration and the physical time derivative is approximated by the three-point backward difference. The turbulence models are switched off to perform a laminar calculation. A structured O-grid of about 130,000 cells is used. No-slip adiabatic conditions are applied at the wall. Pressure is imposed on an arc of the domain boundary in the downstream region of the cylinder. Far-field boundary-conditions are applied on the remaining arc of the boundary domain. Fig. 9 shows the comparison between the results obtained with FaSTAR and those of Giannetti & Luchini [15]. The comparison of the nonlinear Strouhal number evolution with the Reynolds number is

done against [6]. In the left column, the results obtained with FaSTAR nonlinear solver are shown. The top plot shows the separation length, L_{sep}, of the base flow solutions while the bottom plot the Strouhal number of the von Kármán vortex street shedding when unsteady calculations are carried out. The relative percentage error is at worst 1.3%. The middle column reports the Reynolds number evolution of the (top) growth rate and (bottom) Strouhal number predicted by the global stability analysis performed with the linearized solver version of FaSTAR. Excluding the growth rate at $Re = 50$ (the value of σ is small, hence prone to a larger error), the relative percentage error is always below 3%. In the right column, the whole spectrum (top) and the eigen-streamwise velocity corresponding to the unstable mode (bottom) are reported. A satisfactory agreement is obtained for various Reynolds numbers and the laminar part of the linearized solver can be considered validated.

- 2D Turbulent Transonic Buffet

The simulations by Sartor *et al.* [33], carried out on the 2D OAT15A supercritical profile, at different AoA to characterize buffet pre- and post-onset, have been selected. The flow conditions correspond to those in [33] and an OAT15A airfoil with sharp trailing edge and chord of $c = 0.23\,m$ was considered. The geometry used here was however a blunt trailing edge profile. The stagnation pressure and temperature are $101325\,Pa$ and $300\,K$, respectively. The Mach number is $M = 0.73$ and the Reynolds number based on the chord length is $Re = 3.2 \times 10^6$. The numerical fluxes are calculated with the SLAU scheme. The GLSQ is used for the gradient computation. The dual-time stepping method is used to perform an accurate time calculation with an implicit time integration scheme. The LU-SGS scheme is used for the pseudo time sub-iteration and the physical time derivative is approximated by the three-point backward difference. The Spalart-Allmaras turbulence model with rotation correction and quadratic constitutive relation 2000 version is used to close the averaged Reynolds stresses. The trip term ft_2 is also ignored. The boundary conditions used are: no-slip velocity and adiabatic temperature on the profile and far-field boundary conditions are employed at the domain boundaries. The same 2D C-type structured grid counting about 120,000 cells is been used for all AoA. The numerical domain extends about $80c$ above, below and downstream of the profile. The pressure coefficient, C_p, distributions corresponding to the AoA =2.50 (blue), 3.50 (red), 4.50 (black) and 5.50° (magenta) are compared against those of [11, 33] in Fig. 10 (top-left) and show good agreement on both airfoil sides and in terms of shock positions. Contours of the dimensional streamwise velocity for the steady solution at AoA $= 4.50°$ are plotted in Fig. 10 (top-right) along with the sonic (black solid line) and zero-streamwise velocity (white solid line) iso-lines, showing the supersonic flow region/shock position and separation, respectively. The steady solutions are used as base flow solutions for the global stability analysis. Fig. 10 reports the full spectrum (bottom-left) and the unstable eigen-pressure (bottom-right) for the AoA $= 4.5°$ case. Similarly to [33], an unstable mode exists at $St = \approx 0.06$ ($f \approx 75\,Hz$) and the eigenmode is localized on the shock, shock foot and minorily on the mixing layer.

References

[1] Crm.65.airfoil sections [online]. *Available:https://commonresearchmodel.larc.nasa.gov/crm-65-airfoil-sections*, [Accessed 7 March 2017].

[2] E. Akervik, L. Brandt, D. S. Henningson, J. Hoepffner, O. Marxen, and P. Schlatter. Steady solutions of the Navier-Stokes equations by selective frequency damping. *Physics of Fluids*, 18.

[3] W. E. Arnoldi. The principle of minimized iterations in the solution of the matrix eigenvalue problem. *Quarterly of Applied Mathematics*, 9, 1951.

[4] S. Bagheri, E. Åkervik, L. Brandt, and D. S. Henningson. Matrix-free methods for the stability and control of boundary layers. *AIAA Journal*, 45, 2009.

[5] D. Barkley, H. M. Blackburn, and S. J. Sherwin. Direct optimal growth analysis for timesteppers. *International for numerical methods in fluids*, 57:1435–1458, 2008.

[6] D. Barkley and R. D. Henderson. Three-dimensional Floquet stability analysis of the wake of a circular cylinder. *Journal of Fluid Mechanics*, 322:215–241, 1996.

[7] J. D. Crouch, A. Garbaruk, D. Magidov, and A. Travin. Origin of transonic buffet on aerofoils. *Journal of Fluid Mechanics*, 628:357–369, 2009.

[8] J. D. Crouch, A. Garbaruk, and M. Strelets. Global instability in the onset of transonic-wing buffet. *Journal of Fluid Mechanics*, 881:3–22, 2019.

[9] J Dacles-Mariani, G. G. Zilliac, J. S. Chow, and P. Bradshaw. Numerical/experimental study of a wingtip vortex in the near field. *AIAA Journal*, 33:1561–1568, 1995.

[10] J. Dandois. Experimental study of transonic buffet phenomenon on a 3D swept wing. *Physics of Fluids*, 28:016101, 2016.

[11] S. Deck. Numerical simulation of transonic buffet over a supercritical airfoil. *AIAA Journal*, 43(7):1556–1566, 2005.

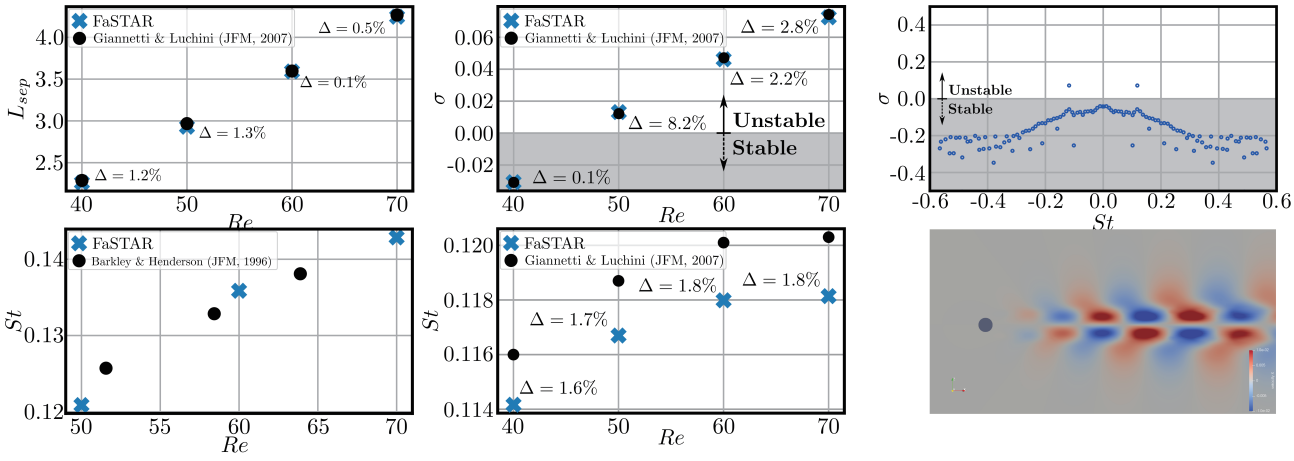

Figure 9: Validation test case: 2D laminar incompressible cylinder.

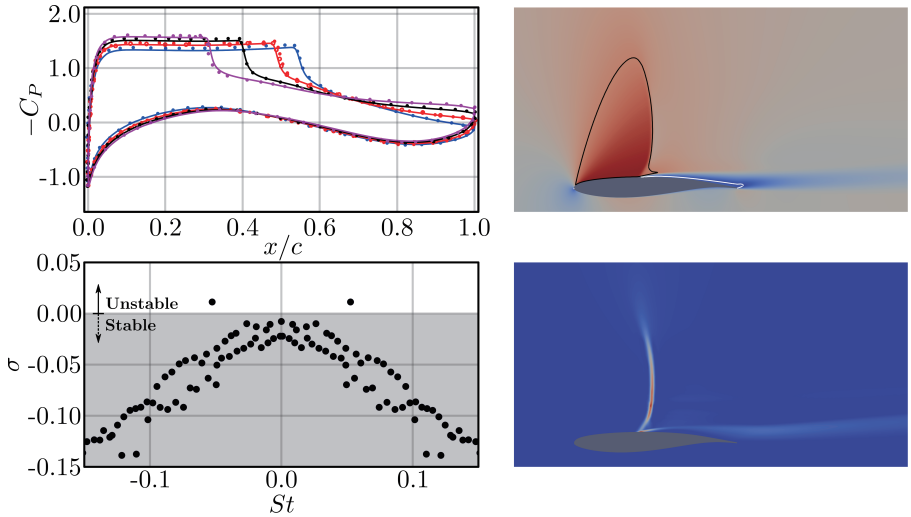

Figure 10: Validation test case: 2D turbulent transonic buffet. In the top-left plot, solid lines correspond to FaSTAR nonlinear solver, full-circles to [33] and empty-circles to [11].

[12] D. Dolling. Fifty years of shock-wave/boundary-layer interaction research: what next? *AIAA Journal*, 39(8):1517–1531, 2001.

[13] W. S. Edwards, L. S. Tuckerman, R. A. Friesner, and D. Sorensen. Krylov methods for the incompressible Navier-Stokes equations. *Journal of Computational Physics*, 110:82–101, 1994.

[14] N. F. Giannelis, O. Levinski, and G. A. Vio. Influence of Mach number and angle of attack on the two-dimensional transonic buffet phenomenon. *Aerospace Science and Technology*, 78:89–101, 2018.

[15] F. Giannetti and P. Luchini. Structural sensitivity of the first instability of the cylinder wake. *Journal of Fluid Mechanics*, 581:167–197, 2007.

[16] F. Grossi, M. Braza, and Y. Hoarau. Prediction of transonic buffet by delayed detached-eddy simulation. *AIAA Journal*, 52:2300–2312, 2014.

[17] F. Guiho, F. Alizard, and J.-C. Robinet. Instabilities in oblique shock wave/laminar boundary-layer interactions. *Journal of Fluid Mechanics*, 789:1–35, 2016.

[18] A. Hashimoto, K. Murakami, T. Aoyama, K. Ishiko, M. Hishida, M. Sakashita, and P. Lahur. Toward the fastest unstructured CFD code 'FaSTAR'. *AIAA Paper 2012-1075*, 2012.

[19] W. F. Hilton and R. G. Fowler. Photographs of shock wave movement. *National Physical Laboratories*, 2692, 1947.

[20] T. Ishida, A. Hashimoto, Y. Ohmichi, T. Aoyama, and K. Takekawa. Transonic buffet simulation over

NASA-CRM by unsteady-FaSTAR code. *AIAA Paper 2017-0494*, 2017.

[21] S. Koike, Y. Matsumoto, and T. Kouchi. Shock-induced separation and shockwave oscillation on swept and unswept two-dimensional common research model wings. In *51st FDC / 37th ANSS Conference*, volume 1A02, 2019.

[22] S. Koike, M. Ueno, K. Nakakita, and A. Hashimoto. Unsteady pressure measurement of transonic buffet on NASA common research model. *34th AIAA Applied Aerodynamics Conference, AIAA AVIATION Forum, AIAA-2016-4044*, 2016.

[23] B. H. K. Lee. Oscillatory shock motion caused by transonic shock boundary-layer interaction. *AIAA Journal*, 28(5):942–944, 1990.

[24] B. H. K. Lee. Self-sustained shock oscillations on airfoils at transonic speeds. *Progress in Aerospace Sciences*, 37:147–196, 2001.

[25] R. B. Lehoucq, D. C. Sorensen, and C. Yang. ARPACK user's guide: solution of large scale eigenvalue problems with implicitly restarted Arnoldi methods. *Technical Note*, 1997.

[26] J.-C. Loiseau, J.-C. Robinet, S. Cherubini, and E. Leriche. Investigation of the roughness-induced transition: global stability analyses and direct numerical simulations. *Journal of Fluid Mechanics*, 760:175–211, 2014.

[27] A. Memmolo, M. Bernardini, and S. Pirozzoli. Scrutiny of buffet mechanisms in transonic flow. *International Journal of Numerical Methods for Heat and Fluid Flow*, 28:1031–1046, 2018.

[28] C. Mettot, F. Renac, and D. Sipp. Computation of eigenvalue sensitivity to base flow modifications in a discrete framework: Application to open-loop control. *Journal of Computational Physics*, 269:234–258, 2014.

[29] S. Obayashi and G. P. Guruswamy. Convergence acceleration of an aeroelastic Navier-Stokes solver. *AIAA Journal*, 33:1134–1141, 1995.

[30] F. Plante, J. Dandois, F. Sartor, and E. Laurendeau. Study of three-dimensional transonic buffet on swept wings. *Proceedings of the AIAA Applied Aerodynamics Conference, Washinton, DC, United States*, 2017.

[31] F. Richez, M. Lequille, and O. Marquet. Selective frequency damping method for steady rans solutions of turbulent separated flows around an airfoil at stall. *Computers and Fluids*, 132.

[32] A. Sansica, J.-C. Robinet, F. Alizard, and E. Goncalvez. Three-dimensional instability of a flow past a sphere: Mach evolution of the regular and hopf bifurcations. *Journal of Fluid Mechanics*, 855:1088–1115, 2018.

[33] F. Sartor, C. Mettot, and D. Sipp. Stability, receptivity, and sensitivity analyses of buffeting transonic flow over a profile. *AIAA Journal*, 53(7):1980–1933, 2015.

[34] F. Sartor and S. Timme. Delayed detachededdy simulation of shock buffet on half wingbody configuration. *AIAA Journal*, 55:1230–1240, 2017.

[35] D. Sharov and K. Nakahashi. Reordering of hybrid unstructured grids for lower-upper symmetric Gauss-Seidel computations. *AIAA Journal*, 36:484–486, 1998.

[36] P. R Spalart. Strategies for turbulence modelling and simulation. *International Journal of Heat and Fluid Flow*, 21:252–263, 2000.

[37] P. R. Spalart and S. R. Allmaras. A one-equation turbulence model for aerodynamic flows. In *30th Aerospace Sciences Meeting and Exhibit, Aerospace Sciences Meetings*, volume AIAA Paper, 1992.

[38] Y. Sugioka, S. Koike, K. Nakakita, D. Numata, T. Nonomura, and K. Asai. Experimental analysis of transonic buffet on a 3D swept wing using fast-response pressure-sensitive paint. *Experiments in Fluids*, 59(108), 2018.

[39] A. Tezuka and K. Suzuki. Three-dimensional global linear stability analysis of flow around a spheroid. *AIAA Journal*, 44, 2006.

[40] S Timme. Global instability of wing shock-buffet onset. *Journal of Fluid Mechanics*, 885, 2020.

[41] M. R. Visbal and R. Gordnier. A high-order flow solver for deforming and moving meshes. volume AIAA Paper 2000-2619, 2000.